Sub-tissue plasmonic heating monitored with $CaF_2:Nd^{3+},Y^{3+}$ nanothermometers in the second biological window

Marta Quintanilla[1]*, Yang Zhang,[2] Luis M. Liz-Marzán[1,3]

[1]CIC BiomaGUNE and CIBER-BBN, Paseo de Miramón 182, 20014 Donostia - San Sebastián, Spain

[2] Electron Microscopy for Materials Science (EMAT), Department Physics, University of Antwerp, Groenenborgerlaan 171, B-2020 Antwerp, Belgium.

[3]Ikerbasque, Basque Foundation for Science, 48013 Bilbao, Spain

ABSTRACT: Measuring temperature in biological environments is an ambitious goal toward supporting medical treatment and diagnosis. Minimally invasive techniques based on optical probes require very specific properties that are difficult to combine within a single material. These include high chemical stability in aqueous environments, optical signal stability, low toxicity, high emission intensity and – essential – working at wavelengths within the biological transparency windows, so as to minimize invasiveness while maximizing penetration depth. We propose $CaF_2:Nd^{3+},Y^{3+}$ as a candidate for thermometry based on an intraband ratiometric approach, fully working within the biological windows (excitation at 808 nm; emission around 1050 nm). We optimized the thermal probes through the addition of Y^{3+} as a dopant, to improve both emission intensity and thermal sensitivity. In order to define the conditions under which the proposed technique can be applied, gold nanorods were used to optically generate sub-tissue hot areas, while the resulting temperature variation was monitored with the new nanothermometers.

Introduction.

Temperature is a critical parameter for life. Both vegetal and animal cells, as well as most bacteria and viruses, can only live and grow within a narrow thermal range. As a consequence, treatments against diseases can be developed, which rely on localized thermal increase (hyperthermia). Temperatures of 5 or 10 ºC above the standard body temperature may be sufficient to cause damage to cells, which can become permanent if exposures are maintained for an extended period of time (one hour or more). If temperature is further increased, it can provoke cell death within few minutes of exposure.[1]

Nanotechnology has provided us with the ability to produce localized hot spots through the use of nanoparticles with heating capabilities, which can be excited remotely, *via* magnetic fields or illumination.[1-2] This is expected to be a valuable, non-invasive therapeutic tool against various diseases, including cancer.[3] However, actual application is limited by the complexity of biological environments, which makes it hard to accurately control the concentration of particles at the infected area, heat diffusion, and the excitation power reaching the spot. As a consequence, the temperature control that can be achieved at the infected area is limited and might become insufficient to achieve the desired effect, or too high, resulting in damage of the surrounding tissue.

Therefore, a great interest has recently emerged on minimally invasive *in situ* thermal monitoring for biomedical applications, involving optical materials with thermometric functionalities. A number of approaches have been proposed for such applications, the main categories comprising optical nanothermometers based on quantum dots, organic molecules (mostly dyes, but also proteins), nanodiamonds and lanthanide-doped nanocrystals.[4-6] In all cases, the selected material is optically excited and then emits light with properties that depend on temperature. Each category presents different pros and cons when it comes to biomedical applications, since these involve a number of requirements that nanothermometers must fulfill, involving biological, chemical and physical limitations.

A key restriction regarding *in vivo* biomedical applications is the penetration depth of light within biological media. Tissues largely absorb and scatter visible light, which as a result cannot travel long within the body (penetration depths of less than a millimeter are often defined for such

cases)[7-8]. A more favorable situation arises when the wavelength lies within the near-IR range. Indeed, three ranges (though recently some more have been proposed, farther in the infrared) have been defined as biological transparency windows: the first one (BW-I) between 750 and 950 nm, the second one (BW-II) between 1000 and 1450 nm, and the third one (BW-III) between 1500 and 1700 nm.[9] The penetration depth of light within these ranges may reach one centimeter (note that the penetration length is an effective value defined to compare the different wavelengths, not the maximum depth that light can reach).[7,10] Regardless of how long light can travel within the medium, it must be considered that the light absorbed by the tissue is transformed mainly into heat released to the environment, thereby modifying its temperature and in some cases damaging it.

Different strategies have been proposed to engineer thermal probes working within the biological windows, to the extent that some of them have even been tested to determine transient temperatures during the study of muscle efficiency,[11] or ischemia diagnosis in live mice.[12] However, very few probes can be used to record absolute temperatures, as this requires a self-referenced technique. The most robust prototypes capable of self-referenced near-IR thermometry are based on measuring temperature through the ratio between two emission intensities, in which one emission can be considered as a probe and the other as the reference. Although, in principle, any two emissions can be used, especially advantageous are those cases in which the emissions are thermally linked to each other. In such cases, the thermal behavior of luminescence can be easily described through a Boltzmann distribution, and such a simple mathematical description largely facilitates the task of exploiting the optical probe to perform accurate sub-tissue measurements.[13]

Aiming at developing high quality nanoparticles that can work in practical sub-tissue experiments, we focused our attention on CaF_2 nanoparticles doped with Nd^{3+}, an outstanding ion for near-infrared thermometry.[14-21] Most ratiometric near-IR thermal probes are based on lanthanide-doped nanoparticles, because their high stability (both chemical and optical) and the characteristics of lanthanide-based luminescence (narrow and well-defined emission bands) are optimal for this application. Yet, for practical implementation, improved luminescence quantum yields are still needed.

It has been recently demonstrated that near-IR emissions are particularly intense in Nd^{3+}-doped CaF_2 or SrF_2 nanoparticles,[17, 22] even when they are dispersed in water (it should be noted that OH^- vibrational modes strongly quench luminescence from lanthanides[23]). Still, since the emission intensity of the probes is directly linked to the thermal resolution of the final thermometry measurements, optimization is required.[16] Since this is particularly relevant for *in vivo* measurements, recent efforts have been made to enhance the emission intensity of lanthanide-doped nanoparticles, either by preparing core/shell structures,[24] or through annealing.[16] We opted for a simpler strategy from the synthesis point of view, which has been previously tested in the field of laser crystals,[25-26] and we are now importing to nanocrystals. The method comprises co-doping of the host with Y^{3+} ions, to avoid clustering and quenching of Nd^{3+} ions. We additionally found that Nd^{3+} emission at 1050 nm is thermally sensitive in CaF2, which is an advantageous characteristic as it is typically more intense than Nd^{3+} emission at 860 nm, more often used in thermometry.[14-19, 21] The performance of the obtained thermal probes with improved emission intensity was tested in *ex vivo* sub-tissue experiments. We monitored plasmonic heating, as a proof-of-concept experiment of photothermal therapy. These experiments were carried out to determine the accuracy of thermal reading, potential sources of error in actual applications and thermal resolution.

Experimental details.

Lanthanide-doped nanoparticles were synthesized following a hydrothermal strategy based on the protocol developed by Pedroni et al.[27] with slight modifications. The starting reagents were neodymium chloride (99.9%, Alpha Aesar) and yttrium chloride (99.99%, Alpha Aesar) as lanthanide sources, calcium chloride (≥ 99%, Sigma-Aldrich) and ammonium fluoride (98+%, Acros) as CaF_2precursors, and sodium citrate tribasic dihydrate (Sigma-Aldrich) as a surfactant. All chemicals were used without further purification, and all experiments were carried out using Milli-Q water. The volume of chlorides containing calcium, neodymium and yttrium was calculated to obtain 3.5 mmol of the final material. Accordingly, the exact amount depends on the concentration of dopants in each case, following the formula $Ca_{1-x-y}F_{2+x+y}:Nd_xY_y$. The mixture of chlorides was dissolved in 10 mL of water, and stirred for 30 min. Then, 10 mL of water containing 5.8 g of sodium citrate was added and the solution was stirred overnight. The resulting milky solution turned transparent upon addition of 7 mL of water containing 324 mg of NH_4F. Fluorine ions are thus in excess during the synthesis. After further stirring for 30 min, the solution was introduced in the Teflon insert (50 mL) of a pressure digestion vessel (DAB-2, Berghof), which was tightly closed to keep the high pressure produced during the reaction. The reactor was then introduced in an oven and kept at 180 ºC for 5 h. After this time, the synthesized

nanoparticles were recovered from the solution by centrifugation (5500 rpm, 12 min), and then redispersed in water, sonicated, and washed twice by centrifugation in acetone.

The concentration of particles in the characterized solutions was determined by ICP, using the particle size estimated from TEM images (JEOL JEM-1400PLUS). Prior to ICP measurements, 100 µL of the particles aqueous solution was digested overnight in 10 mL HNO_3 (65%, Scharlau) at 70 °C. Water was then added to reach 5% concentration of HNO_3. The crystal phase of the nanoparticles was determined by X-ray diffraction (XRD) (PANalytical Xpert PRO) in Bragg-Brentano geometry, using 40 KV and 40 mA in the generator. High resolution HAADF-STEM experiments were performed on FEI Titan 60-300 electron microscope.

The optical characterization of the emission was carried out under laser illumination using a fiber-coupled 808 nm diode laser (Lumics, LU808T040). Light was collimated at the exit of the fiber to a 3 mm diameter beam. The sample luminescence was cleaned with a longpass filter (850 nm cut-on) to remove any laser background, collected with a fiber and recorded with an InGaAs spectrometer (Sol 1.7, B&WTek). For thermal calibration, the sample was kept in a copper-aluminum holder that fully covered an optical-glass cuvette (Hellma). The sample was heated on a hot-plate, and temperature was measured with a type K thermocouple placed inside the solution.

For *ex vivo* experiments (based on chicken breast), the optical set-up was using the same components, though temperature was additionally monitored using a thermal camera (FLIR A35). We selected chicken breast as standard model tissue. The thickness of the piece of tissue was measured precisely on the spot where laser light would hit it (laser spot was 3 mm diameter) using thermal camera images. An aqueous nanoparticles dispersion (16 µg/mL) was placed in a cuvette right behind the tissue, and luminescence was recorded back on the surface with a detector placed at 45º with respect to the illumination axis. For this experiment, we used nanoparticles doped with $[Nd^{3+}]$ = 1 mol% and $[Y^{3+}]$ = 10 mol%. Spectra were recorded at different excitation powers between 250 mW and 1.2 W for each chicken breast thickness. An exponential trend was obtained for each illumination power versus tissue thickness, which was then normalized, so all of them showed the same trend and could be averaged to determine the uncertainty in intensity. The experiment was finished at the thickness in which the lower excitation power did not provide a sufficiently bright emission to record a meaningful spectrum. It should be noted that the process of recording full spectra (including integration and averaging) was set to less than 15 seconds per spectrum, so the whole set of spectra were recorded fast enough to avoid any effect due to chicken breast dryness.

Gold nanorods were prepared using the seeded growth method with some modifications, as previously described by Scarabelli et al.[28] and further developed by González-Rubio et al.[29] As starting materials, 5- bromosalicylic acid (BrSal, technical grade, 90%), hydrogen tetrachloroaurate trihydrate ($HAuCl_4{\cdot}3H_2O$, ≥99.9%), Hexadecyltrimethylammonium bromide (CTAB, ≥99%), silver nitrate ($AgNO_3$, ≥99.0%), L-ascorbic acid (≥99%), and sodium borohydride ($NaBH_4$, 99%) were purchased from Aldrich. Sodium oleate (NaOL, > 97.0%) was purchased from TCI America. Nanopure water (resistivity 18.2 MΩ·cm at 25 °C) was used in all experiments. All starting materials were used without further purification. Seeds were prepared by the standard CTAB/$NaBH_4$ procedure, by adding 25 µL of a 0.05 M $HAuCl_4$ solution to 4.7 mL of a 0.1 M CTAB solution. Then, under vigorous stirring, 300 µL of a freshly prepared 0.01 M $NaBH_4$ solution was injected. Prior to use, excess borohydride was consumed by ageing the seed solution for 30 min at room temperature. To prepare 50 mL of gold nanorods solution, 45 mg of 5-bromosalicylic acid was added to 50 mL of 0.05 M CTAB and the mixture was gently stirred for 15 min until complete dissolution. Next, 480 µL of 0.01 M $AgNO_3$, 200 µL of 0.1 M ascorbic acid, and 500 µL of a 0.05 M HAuCl4 solution were added to the mixture. The solution was kept at 25 °C for 2 h (or until Au (III) was completely reduced to Au (I) by BrSal, which can be monitored by a decrease in the absorbance of the Au(III) CTAB complex at 390 nm). Then, 50 µL of a 0.1 M ascorbic acid solution was added under vigorous stirring, followed by 80 µL of the seed solution. The mixture was left undisturbed at room temperature for at least 2 h. The resulting gold nanorods displayed LSPR maxima ranging from 820 to 890 nm. To obtain an LSPR at 810 nm the obtained gold nanorods were overgrown at room temperature for 4 h in the presence of ascorbic acid. The optimum amount of ascorbic acid can be found experimentally by overgrowing small aliquots of the prepared nanorods with increasing volumes of the ascorbic acid solution (from 0.3 to 0.6 µL per mL).

Once the full process was completed, the gold nanorods were washed and purified by centrifugation (50 mL at 8000 rpm, 30 min). The precipitate was redispersed in the same volume of a 0.002 M CTAB solution. Centrifugation was repeated twice and the particles were redispersed in 5 mL of a 0.001 M CTAB solution. The nanorods used in this work were 68 ± 6 nm long by 18 ± 1 nm wide.

Results and discussion.

Definition and optimization of the thermometer

CaF_2 nanoparticles were synthesized following a hydrothermal route previously developed by Speghini and co-workers.[27] This approach is characterized by the use of mild temperatures and by the dispersibility of the resulting particles in water, with no need for further modification. We obtained nanoparticles with a cubic morphology, as can be appreciated in the TEM image of Figure 1A. All preparations resulted in particles with size distributions that could be fit to a Log-normal function (Figure S1, Supporting Information). The average particle size, measured from the diagonal dimension of the cube faces, varied slightly for different batches, as shown in Table 1 below. However, such differences were negligible when considering the standard deviation, so we can safely state that the diagonal dimension of the nanoparticles was 12±3 nm. The crystallographic structure was further analyzed by STEM (Figure 1B). The high resolution of this technique allowed us to determine the lattice spacing, which appears to be consistent with the cubic structure of CaF_2 (a = 5.451 Å), though slightly distorted as usually observed for doped materials. XRD measurements were additionally performed for all batches (Figure 1C), so as to confirm that the obtained material was CaF_2 and no additional crystal phases were observed.

Nd^{3+} doping of the nanocrystals provides CaF_2 with energy states that allow optical excitation in the near-IR, around 800 nm, as well as light emission at longer wavelengths. The inset in Figure 2 shows a partial energy-states diagram for Nd^{3+} ions. As labeled, the transition $^4I_{9/2} \rightarrow {}^4F_{5/2}, {}^2H_{9/2}$ is responsible for the absorption at 800 nm. Given the close distance to the immediate lower level, $^4F_{3/2}$, this can be populated following a non-radiative route that depopulates $^4F_{5/2}, {}^2H_{9/2}$. The main emissions of Nd^{3+} in the near-IR are related to radiative relaxations of this energy state to lower levels, the most intense being $^4F_{3/2} \rightarrow {}^4I_{11/2}$, between 1000 and 1130 nm (see spectrum in Figure 2). It should be noted that $^4F_{3/2}$ is split in two different sublevels, R_1 and R_2, due to the effect of the crystal field. Accordingly, the separation between both sublevels depends on the direct environment of Nd^{3+} ions, and thus is different for each optical center present in the material. The emission band observed is therefore a convolution of all the different emission lines produced by the specific mix of optical centers (and defects) in each crystal.

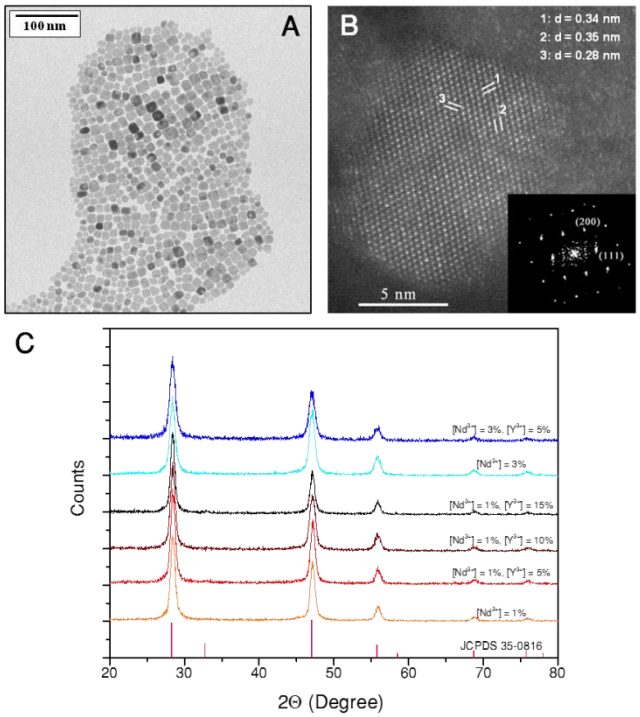

Figure 1. (A) TEM micrograph of synthesized CaF_2 nanoparticles. (B) HAADF-STEM image of the particles showing their crystalline structure and lattice spacing, evidenced by the inserted FFT pattern. (C) XRD patterns of the synthesized samples, featuring diffraction lines in agreement with those expected for CaF2 (JCPDS 35-0816).

We were interested in specifically developing a thermometer for biological applications, thus operating within the near-IR transparency windows of biological tissues. The excitation scheme used to obtain the emission spectrum in Figure 2 is optimal, as the excitation wavelength lies within the first biological window and the main emission band fits the second biological transparency window.

A thermometer is defined in general by its sensitivity, *i.e.* the rate of change of the parameter used as sensor versus temperature. However, in practice, this is not the only relevant figure of merit. In the case of an optical thermometer, the intensity of the signal (and the quality of the light detection system) may play a role in limiting the signal-to-noise ratio which is reflected in the resolution of the measured temperature. Therefore, we focus on the most intense emission band at ~1050 nm, rather than using the most usual one at ~850 nm. Prior to defining the thermometer we tried to improve the signal intensity. In recent studies of CaF_2:Nd^{3+} as a laser material (Nd^{3+}-doped CaF_2 bulk crystals), it has been reported that co-doping of Nd^{3+} with different ions such as Y^{3+}, La^{3+} or Sc^{3+}, has a positive effect on the emission intensity of Nd^{3+}.[25] We thus

imported this strategy to our nanomaterials and studied its implication in nanothermometry.

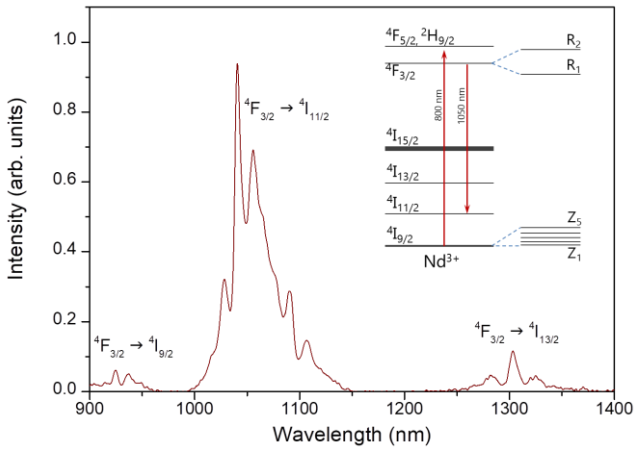

Figure 2. Emission spectrum of Nd^{3+}-doped CaF_2 nanoparticles, excited at 808 nm. The main Nd^{3+} emissions are labeled according to the related transitions. The inset shows a partial energy diagram of Nd^{3+} energy states.

The reasoning behind the effects of co-doping on the emission intensity is based on the defects structure of CaF_2. The lattice of CaF_2 comprises fluorine atoms at the corners of cubes that are alternately filled with a calcium atom (Figure 3A). When Nd^{3+} ions are incorporated into the structure, they replace Ca^{2+} ions and as a consequence introduce excess positive charge. A charge compensation mechanism is then needed to maintain the electrical neutrality of the system. The most common mechanism involves introducing a fluorine ion at an interstitial site (Figure 3B).[25, 30] From the point of view of the optical properties, the location of this interstitial fluorine is relevant, as it modifies the environmental crystal field of Nd^{3+}. Indeed, in those cases in which the interstitial fluorine ion is far away from the Nd^{3+} ion, the optical site has a highly symmetric cubic distribution (O_h), in which $4f \rightarrow 4f$ transitions typical of lanthanide ions are parity forbidden. However, such transitions become partially allowed in asymmetric fields. When fluorine ions are close enough to Nd^{3+}, Nd^{3+}-F^- emitting pairs are created. The most common Nd^{3+}-F^- emitting pair is the one shown in Figure 3B, which displays C_{4v} symmetry.[30-33] Interstitial fluorine is thus responsible for the existence of differentiated optical centers and causes inhomogeneous broadening of the emission bands.

The concentration of O_h sites is higher at very low Nd^{3+} concentrations. On increasing Nd^{3+} concentration, Nd^{3+}-F^- pairs gain relevance, and at even higher concentrations they start clustering to form larger groups (Figure 3C), known as M centers if two pairs are involved, or N centers if they involve three pairs.[31, 33] In CaF_2 clustering occurs at rather low Nd^{3+} concentrations (in the order of 1 mol%) and it is detrimental for the emission intensity of the material, because Nd^{3+} ions get close enough to each other and favor non-radiative transitions over radiative ones.

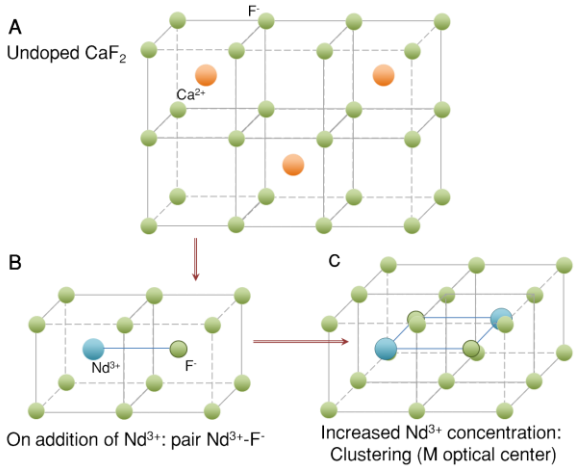

Figure 3. (A) Scheme of the cubic lattice of CaF_2. (B) When Nd^{3+} ions are added, they replace Ca^{2+} ions, which requires the presence of a fluorine ion at an interstitial position. (C) Upon increasing Nd^{3+} concentration, clusters of Nd^{3+}-F^- pairs are formed.

Non-radiative relaxation paths (migration) can be hindered through the addition of Y^{3+} ions that can participate in the clusters, thereby increasing Nd^{3+} emission intensity. To exploit this effect, we prepared a series of nanoparticles with different concentrations of Nd^{3+} (1% and 3%) and Y^{3+} ions (from 0 to 15%) and studied their emission to find out to what extent the intensity can be improved in the nanoparticles. Figure 4A shows the emission spectra of the different samples dispersed in water. In order to do the comparison, the concentration of Nd^{3+} ions, measured by ICP-MS, was kept constant. Therefore, the concentration of particles with 3% Nd^{3+} is lower than that of 1% Nd^{3+} particles. This is however a fair way to determine to what extent Nd^{3+} ions are quenched. To help understanding the result, the inset of Figure 4A presents a plot of the integrated intensity of the emission band *vs.* Y^{3+} concentration. In the case of 3% Nd^{3+}, addition of Y^{3+} resulted in a change of lineshape in the emission band, but only a moderate change in intensity. Instead, in the case of 1% Nd^{3+} the difference is obvious, both regarding intensity and lineshape. Indeed, we measured a five-fold increase in emission intensity for the sample containing 15% Y^{3+} as compared to the sample with no Y^{3+}.

The change in emission lineshape can be related to a modification of the direct environment around Nd^{3+} ions and to a different distribution of optical centers between the different particles, which is thus consistent with the previously described structure of defects in Nd^{3+}-doped

CaF_2. Considering all the different samples, three main emission lines can be readily differentiated, at 1041, 1053 and 1062 nm, consistent with previous reports on this material,[34] but we can also see in the spectra additional contributions to the emission. To better observe the differences in lineshape, the normalized emission spectra are plotted in Figure 4B, 4C. We can see that, at low Y^{3+} concentrations, the main contribution is related to the 1041 nm peak, whereas the emissions at longer wavelengths gain intensity when increasing the amount of Y^{3+} present in the crystal.

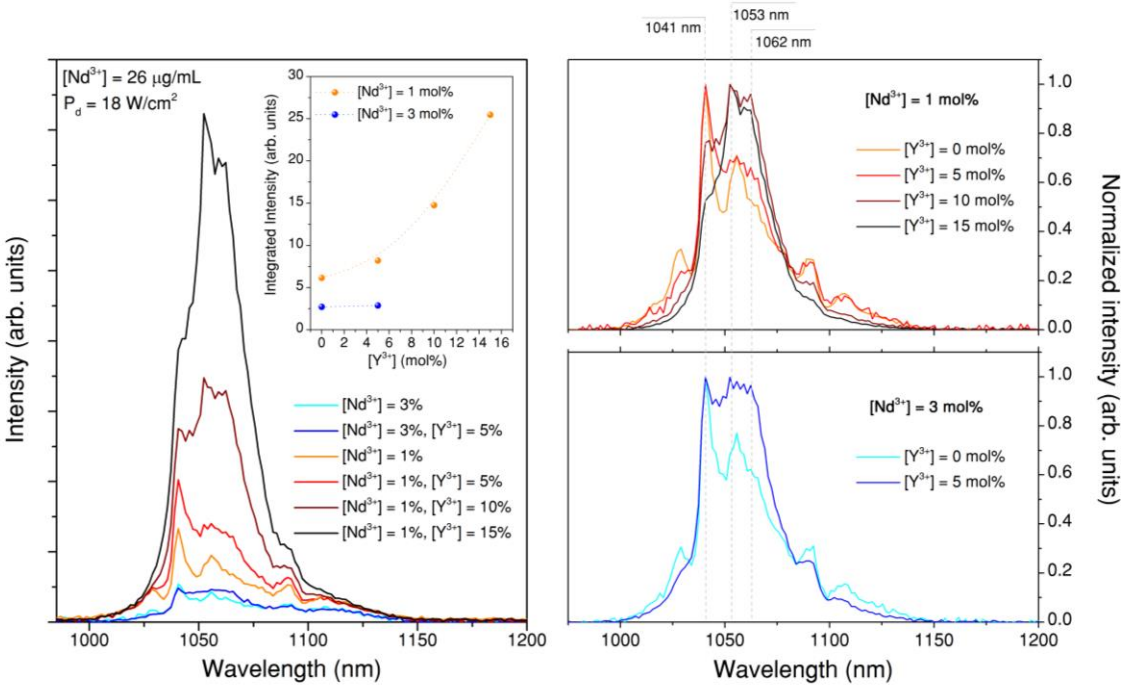

Figure 4. (A) Emission of Nd^{3+} ions ($^4F_{3/2} \rightarrow {}^4I_{11/2}$ transition) upon excitation at 808 nm, for samples synthesized with different Nd^{3+} and Y^{3+} concentrations. The solutions were prepared to keep a constant concentration of Nd^{3+} ions. (B,C) Addition of Y^{3+} leads to changes in the spectral line-shape of the emission, affecting the ratio between the peak at 1041 nm and those at 1053 and 1062 nm.

Table 1. Size and thermal calibration values of the different samples, including their relative thermal sensitivity.

Dopants Concentration		Size	Ratio		Ln(B)	ΔE	S_R (%K^{-1})
Nd^{3+} (mol%)	Y^{3+} (mol%)	(diagonal, nm)	I_1	I_2		(cm^{-1})	At 300 K
1	0	15 ± 3	1041	1062	-0.23 ± 0.01	75 ± 3	0.12
1	5	10 ± 3	1041	1062	-0.37 ± 0.04	70 ± 8	0.11
1	10	12 ± 3	1041	1062	-0.57 ± 0.03	98 ± 6	0.16
1	15	14 ± 3	1053	1062	-0.15 ± 0.01	49 ± 3	0.18
3	0	11 ± 3	1041	1062	-0.29 ± 0.03	78 ± 6	0.13
3	5	10 ± 2	1041	1062	-0.43 ± 0.03	82 ± 5	0.13

These changes have relevant consequences from the thermometry point of view. As mentioned above, an optical thermometer can be defined using any feature of the emission that can be linked to temperature. Aiming to get a self-referenced system, we chose to define a thermometer based on the intensity ratio between two different emission peaks. Intensity ratios involve measuring light emission at two different wavelengths, and

then comparing their intensities. In the ideal situation, both emissions should be close to each other and hence the extinction coefficient of the environment would have a similar effect at both wavelengths, thereby avoiding inaccuracy in the thermal reading. Still, this may be a source of error which we analyze below, and which can be easily evaluated if both emissions correspond to thermally linked states and thus share electronic populations.[10] Such a population share occurs when both emission states are close to each other, so that electrons can populate the upper level from the lower state thanks to thermal energy. The fluorescence intensity ratio (*FIR*) is then described by a Boltzmann distribution:

$$FIR = \frac{I_1}{I_2} = B\ exp\left(-\frac{\Delta E}{k_B T}\right) \quad (1)$$

where I_1 and I_2 are the intensities associated to the upper and lower states, respectively, k_B is Boltzmann's constant, T is the temperature and ΔE is the energy gap separating both emitting states, and is thus a property of the material. Finally, B is a constant given by:

$$B = \frac{c_1(\nu) A_1 g_1 h\nu_1}{c_2(\nu) A_2 g_2 h\nu_2} \quad (2)$$

where A_i (i = 1, 2) and g_i are the spontaneous emission rates and degeneracies of the multiplets, $c_i(\nu)$ is the spectral response of the experimental system at the emission frequency ν_i, and h is Planck's constant.[35] It should be noted that in situations at which the environment is not transparent at ν_i, $c_i(\nu)$ must also include a contribution dependent on the extinction coefficient of the environment.

In the present case, the intensity ratio can be set between emissions linked to transitions starting at sublevels R_1 and R_2 (Figure 2). This is between the peak at 1041 nm (I_1) and those at longer wavelengths. For the largest Y^{3+} concentration though, this ratio loses significance due to the lower intensity of the 1041 nm peak (Figure 4B), and thus the thermometer must be defined between the 1053 nm (I_1) and the 1062 nm (I_2) emissions (Table 1). Note that each intensity ratio is not calculated from the maximum intensity of each peak, but from the integrated area below the whole emission peak.

When writing equation (1) in a logarithmic form, it becomes $\ln(I_1/I_2) = \ln B - \Delta E/k_B T$, which can be understood as a linear function of $1/T$; the slope being given by $\Delta E/k_B$ and the intercept by lnB. Figure 5A shows the calibration curves for the different samples, based on the defined ratios. The fitting parameters are provided in Table 1. This shows that for most samples the main difference in the calibration curve is lnB, but the slope is largely the same. Considering the error in the fittings, the average value of ΔE is 80 ± 10 cm^{-1}. The only exception is the sample with the higher Y^{3+} content ([Nd^{3+}] = 1%, [Y^{3+}] = 15%), since the strong variation in lineshape required changing the definition of the intensity ratio.

The sensitivity (S) is a figure of merit of the thermometer, defined as the variation of the measuring parameter with temperature, i.e. $S = |\partial FIR/\partial T|$. In order to facilitate comparison between different types of thermal sensors, sensitivity is often normalized to provide a value with dimensions that are independent of the thermal parameter. This gives rise to a relative sensitivity:

$$S_R = \left|\frac{1}{FIR}\frac{\partial FIR}{\partial T}\right| = \frac{\Delta E}{k_B T^2} \quad (3)$$

where equation (1) has already been differentiated in the last term. Unlike absolute sensitivity, S_R only depends on the energy gap between both levels involved (ΔE), since normalization removes all dependences on the constant B. However, B is related to properties of the material, such as the spontaneous emission rate, which plays a role in the *FIR* vs. temperature trend. Since B may also change with the experimental conditions, absolute sensitivity is not an exportable parameter, while S_R can be exported.

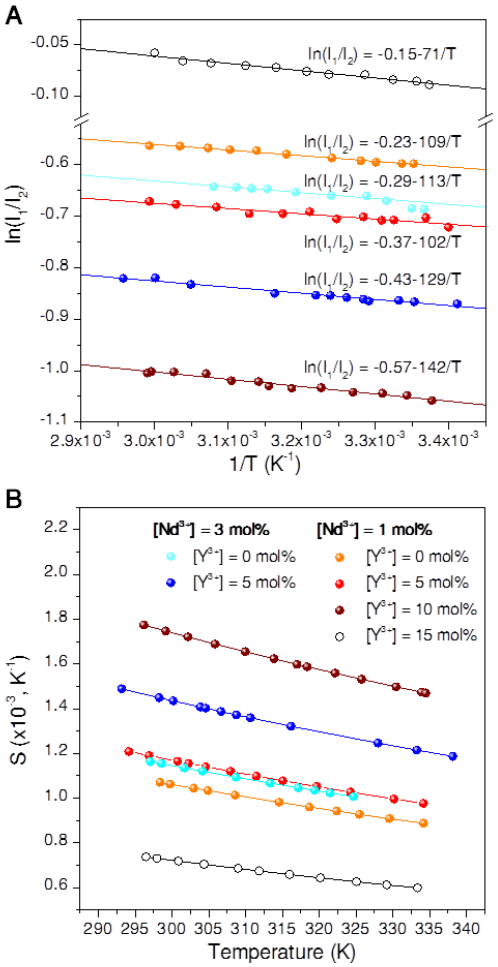

Figure 5. (A) Thermal calibration of particles synthesized with different concentrations of Nd^{3+} and Y^{3+}, plotted as $\ln(I_1/I_2)$ *vs.* 1/T, so the experimental dots can be fit with a straight line. The lines represent the best fit, given by corresponding equation. (B) Calculated sensitivity, S, for each CaF_2:Nd^{3+}, Y^{3+} sample.

All the samples considered here were measured under identical conditions, and thus we can use the absolute sensitivity (plotted in Figure 5B) as a parameter to compare the response of all our thermometers. To allow comparison with other works, the values obtained for the relative sensitivity at 300 K are provided in Table 1. As shown in Figure 5B, we find a moderate variation in the absolute sensitivity of the thermometers with varying concentration of dopants. Still, we see a growing trend with yttrium concentration, at least up to the point at which the intensity ratio must be redefined due to line-shape changes, as previously discussed. These sensitivity values lie within the range typically found for Nd^{3+}-doped thermometers.[36]

Considering the emission intensity (Figure 4A) together with the thermal sensitivity (Figure 5B), an optimal concentration of $[Y^{3+}]$ = 10 mol% is found for a given concentration of $[Nd^{3+}]$ = 1 mol%, which provides the best combination of sensitivity and intensity. For higher yttrium concentrations, the thermal sensitivity decreases, while for lower concentrations emission intensity is weaker. Indeed, thermal resolution, ΔT_{min}, is by definition the smallest change in temperature that causes a perceptible change in the measured *FIR*, and is given by:

$$\Delta T_{min} = \frac{\Delta FIR}{S} \quad (4)$$

where ΔFIR is the uncertainty of the measurement. From this definition it is clear that the thermal resolution will vary for each particular application, but good signal-to-noise ratios will consistently be related to small ΔFIR, and thus to better resolutions. Accordingly, in situations where signal-to-noise ratios may require further improvement, an increase in intensity due to a higher yttrium concentration may compensate for the lower sensitivity.

***Ex vivo* experiments:**

The intensity of light travelling through a medium can be assumed to decay exponentially in the direction of light propagation. Penetration depth is then defined as the characteristic distance of the exponential decrease (the distance at which normalized intensity decays to 1/e).[7] Typically, the penetration depth of light within biological tissues depends on the type of tissue and the illuminating conditions (wavelength, spot-size).[37-38] Taking *ex vivo* human muscle tissue as an example, penetration depth may vary from ~ 1.5 mm for red wavelengths, up to 3 - 4 mm for 835 nm illumination.[8] These values serve as a reference for cases in which light travels through tissue. However, if we intend to develop minimally invasive thermometry techniques, light must travel twice through the tissue, first during excitation (808 nm) and then during emission (1050 nm). Therefore, penetration depth will have a double contribution.

To study the penetration depth when using CaF_2:Nd^{3+},Y^{3+} nanothermometers, we selected chicken breast as an *ex vivo* model, which was cut in pieces of different thicknesses for this study. We selected as nanothermometers the particles doped with 1 mol% Nd^{3+} and 10 mol% Y^{3+}, as they displayed the best thermal sensitivity and good emission intensity. An aqueous dispersion of nanoparticles (0.16 wt%) was placed in a cuvette right behind the chicken tissue, and luminescence was recorded back on the surface (See scheme in Figure 6). After measuring the signal intensity for several values of tissue thickness, the integrated emission intensity reaching the detector was normalized to the value obtained when no tissue was present.

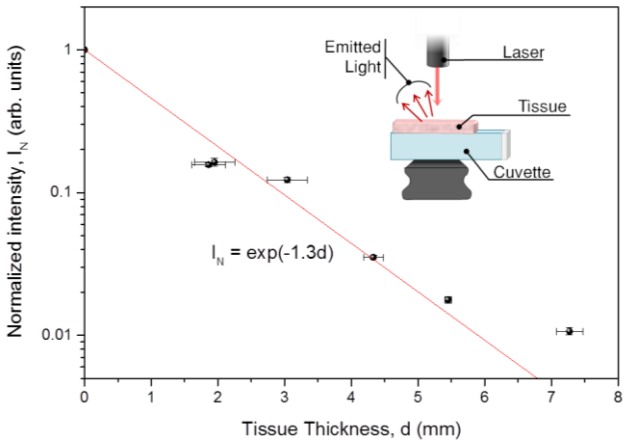

Figure 6. Logarithmic plot of normalized intensity versus the tissue thickness. Experimental data were fitted with an exponential decay (red line). The errors in thickness are given by the apparent heterogeneity of the pieces of tissue. The errors in intensity correspond to the standard deviation from five different spectra. The inset is a scheme of the experimental set-up.

In Figure 6 the measured intensity from Nd^{3+} at different thicknesses is presented as a logarithmic plot, which could be fitted with an exponential decay, obtaining a penetration depth of 1.3 ± 0.1 mm. The maximum tissue thickness that we can use while still having a meaningful signal depends on additional experimental aspects, such as excitation power and detector quality. As mentioned above, penetration depth also varies with beam size, as the contribution of scattering at the center of the spot in a

dense medium is less critical for wider beams than on the edges.[38] In our case, with the lowest excitation power applied (250 mW) in a 3 mm wide beam, we could record the emission from as deep as 7 mm.

One of the main biomedical applications in which nanothermometry can be exploited is photothermal therapy. The treatment requires incorporation of a heating element to produce localized heat. To test the possibility of carrying out monitored photothermal treatment, we used gold nanorods, which upon excitation of their longitudinal plasmon mode can efficiently trigger a thermal increase.[39] We thus synthesized gold nanorods with an LSPR maximum at 810 nm (Figure 7A), matching the excitation wavelength required for our thermometers, and thus keeping overall operation in the near-IR. Gold nanorods were mixed with $CaF_2:Nd^{3+},Y^{3+}$ (1 %, 10%) in a cuvette, by which we expected to optically monitor through the tissue the temperature generated in the cuvette ([Au] in the cuvette was 1.3×10^{-3} mM, calculated from ICP-MS elemental analysis. A more detailed description of the mixed solution is provided in the Supplementary Information). In this experiment we used a thermal camera to obtain a second temperature reading, but it should be noted that the camera has an accuracy of ±5°C. As an example of the measurements, we show in Figure 7B the images obtained for three different pieces of tissue illuminated at 808 nm with 710 mW laser power. The solution containing gold nanorods and CaF_2 nanoparticles was found to get warmer along the laser path. Instead, the tissue did not present any major heating, apart from a slight effect due to heat dissipation from the cuvette. These images support our hypothesis that temperature should be monitored *in situ* during photothermal therapy to optimize the treatment, as the external temperature is significantly different.

Before proceeding with the experiments, a preliminary measurement was performed to study the effect of the laser beam on tissue only (See Figure S2 in the Supporting information). Following this test, we decided to keep the laser power below 0.94 W in order not to overheat the tissue. A second preliminary experiment was performed to check if any heating was caused in the solution by the thermometric particles alone (see Supporting Information, Figure S3). This study was motivated by former works that demonstrate in several hosts that high concentrations of Nd^{3+} ions can trigger a thermal increase.[1] In the present case, our results show that heating due to $CaF_2:Nd^{3+}$,Y^{3+} (1%, 10%) is negligible.

High precision temperature measurements based on $CaF_2:Nd^{3+},Y^{3+}$ luminescence require a good signal-to-noise ratio in the recorded spectra. We are however limiting the excitation power to avoid overheating of the tissue, as explained above. We used integration times and averaging to keep the measurement recording time below 15 s, so as to avoid dehydration of the *ex vivo* tissue. Under these experimental conditions, we proceeded to determine the temperature of the solution through pieces of tissue of different thickness up to 7 mm. The obtained values are shown in Figure 8 and compared to those provided by a thermal camera. We can see that the values obtained from both thermometry systems present a very good agreement up to a penetration of 5.5 mm, thereby demonstrating the accuracy of the proposed optical system to measure through biological tissues. Within the experimental constrains discussed above, the signal-to-noise ratio of the spectrum recorded below 7 mm thick tissue does not allow for a reliable thermal reading.

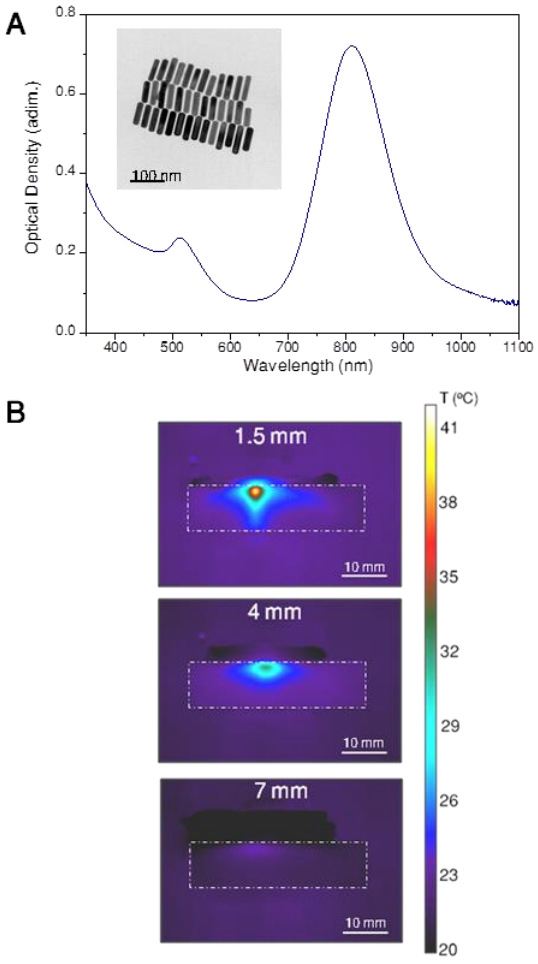

Figure 7. (A) Extinction spectrum of a colloid of gold nanorods used as optical heaters. The inset shows a representative TEM image. (B) Thermographs of a cuvette containing gold nanorods and $CaF_2:Nd^{3+}$, Y^{3+} nanoparticles vertically illuminated with a laser at 808 nm (710 mW, beam diameter 3 mm) after the beam passed a piece of tissue of 1.5,

4 or 7 mm (which appears mainly black in the images). The edges of the cuvette are indicated by a dashed white line for the sake of clarity.

The calculation of temperature from the particles luminescence, as shown in Figure 8, was carried out using the calibration presented in Figure 5 with a required modification. From equation (1) the calibration depends on two different parameters, ΔE and B. In principle, ΔE is not expected to change when the particles´s environment changes. However, as expressed in equation (2), B may suffer from some differences through $c_i(v)$. Supporting this claim, Balabhadra et al. recently pointed out that B needs to be corrected when the particles are transferred between different solvents. Fortunately, a complete recalibration is not required, but it is sufficient to measure several spectra at different excitation powers.[13] A linear fit to the data then allows us to calculate the intensity ratio at zero power, which can be assumed to be the value of FIR at room temperature (see the Supplementary Information for a detailed description). Accordingly, B can be deduced using equation (1). In sub-tissue measurements like those presented in Figure 8, this correction is required for the sake of accuracy, and it gains even more relevance when the particles are deeper within the tissue. Indeed, for the variations in lnB found between the different experimental situations studied here (Supporting Information, Figure S4) a miscalculation in temperature of tens of degrees is expected for a fixed typical value of FIR and ΔE.

Finally, it should be noted that the thermal resolution (equation (4)) obtained from $CaF_2:Nd^{3+},Y^{3+}$ nanoparticles changes with the measurement conditions through ΔFIR and with the environmental temperature through S. The thermal resolution achieved in each case is given as the error bars in Figure 8, and varies from ~0.2 °C for a tissue thickness below 2 mm, to ~3.5 °C for the values measured behind 5.5 mm of tissue.

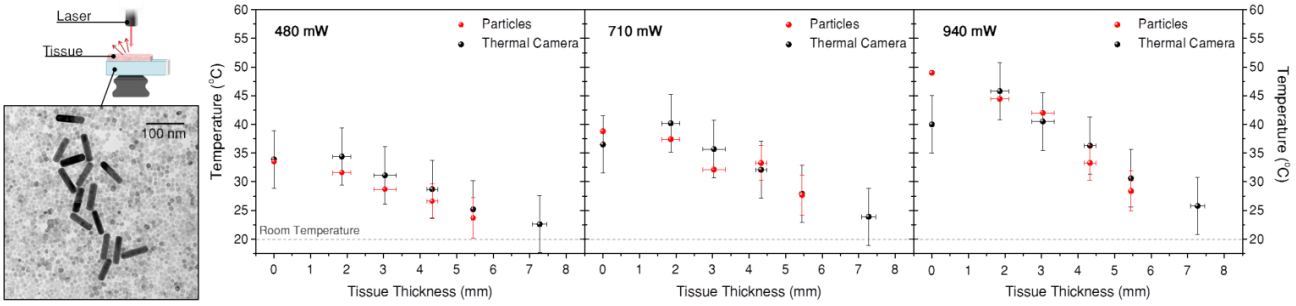

Figure 8. Temperature determined in sub-tissue measurements using a colloidal solution containing gold nanorods and $CaF_2:Nd^{3+}$, Y^{3+} nanoparticles (a TEM image of the mixed colloid is shown on the left). Temperature was determined from the side using a thermal camera (black dots) and through the tissue using the luminescence of Nd^{3+} (red dots). The y-axis error bars account for the accuracy of the thermal camera (black) and the thermal resolution of the optical nanothermometers (red) in each case.

Conclusions

$CaF_2:Nd^{3+},Y^{3+}$ nanoparticles are proposed as optical thermal probes, fully working within biological transparency windows (808 nm excitation wavelength; ~1050 nm emission wavelength). In the nanoparticle design, Nd^{3+} ions are the optically active ions, whose emission is directly related to temperature, while Y^{3+} ions help breaking those migration processes between Nd^{3+} ions that reduce emission intensity. However, the presence of Y^{3+} also modifies the emission lineshape at 1050 nm, to the extent that the most convenient intensity ratio to be used as a thermometer cannot be defined above a certain concentration. This leads to an optimal nanoparticle design in terms of both sensitivity and emission intensity, with $[Nd^{3+}]$ = 1 mol% and $[Y^{3+}]$ = 10 mol%. Such nanoparticles were tested for sub-tissue thermometry experiments, in which a hot volume was generated using gold nanorods as nanoheaters. In order to implement nanothermometers in biological experiments, various practical aspects were considered, including the effect of excitation power on tissue, limited spectral recording parameters and the required correction of the thermal calibration, to account for the absorbance of the tissue at different wavelengths. The thermal resolution obtained in such experiments was found to strongly depend on tissue thickness and other experimental constrains, varying between 0.2 and 3.5 °C in our specific experimental set-up.

AUTHOR INFORMATION

Corresponding Author

*E-mail: mquintanilla@cicbiomagune.es

Author Contributions

The manuscript was written through contributions of all authors. All authors have given approval to the final version of the manuscript.

ACKNOWLEDGEMENTS

The authors would like to thank Dr. Guillermo González Rubio for his kind support with the synthesis of gold nanorods.

M.Q. and L.M.L.-M. acknowledge financial support from the European Commission under the Marie Sklodowska-Curie program (H2020-MSCA-IF-2014_659021 - PHELLINI).

Yang Zhang acknowledges financial support from the European Union's Horizon 2020 research and innovation programme under the Marie Skłodowska-Curie grant agreement No 665501 through a FWO [PEGASUS]² Marie Skłodowska-Curie fellowship (12U4917N).

SUPPORTING INFORMATION

The Supporting Information is available free of charge on the ACS Publications website at DOI: 10.1021/acs.chemmater.xxxxx.

Further information on the size distribution of the prepared nanoparticles, a detailed description of the calculation of B in sub-tissue experiments and information of the heating ability of CaF2 nanoparticles.

REFERENCES

1. Jaque, D.; Martinez Maestro, L.; del Rosal, B.; Haro-Gonzalez, P.; Benayas, A.; Plaza, J. L.; Martin Rodriguez, E.; García Solé, J., Nanoparticles for photothermal therapies. *Nanoscale* **2014,** *6*, 9494-9530.

2. Deatsch, A. E.; Evans, B. A., Heating efficiency in magnetic nanoparticle hyperthermia. *J. Magn. Magn. Mater.* **2014,** *354*, 163-172.

3. Jha, S.; Sharma, P. K.; Malviya, R., Hyperthermia: role and risk factor for cancer treatment. *Achiev. Life Sci.* **2016,** *10*, 161-167.

4. Brites, C. D.; Lima, P. P.; Silva, N. J.; Millán, A.; Amaral, V. S.; Palacio, F.; Carlos, L. D., Thermometry at the nanoscale. *Nanoscale* **2012,** *4*, 4799-4828.

5. Jaque, D.; Vetrone, F., Luminescence nanothermometry. *Nanoscale* **2012,** *4*, 4301-4326.

6. Quintanilla, M.; Liz-Marzán, L.M. Guiding Rules for Selecting a Nanothermometer. *Nano Today*, doi: 10.1016/j.nantod.2018.02.012.

7. Yoon, G.; Welch, A. J.; Motamedi, M.; van Gemert, M. C. J., Development and application of three-dimensional light distribution model for laser irradiated tissue. *IEEE J. Quantum Electron.* **1987,** *QE-23*, 1721-1733.

8. Stolik, S.; Delgado, J. A.; Pérez, A.; Anasagasti, L., Measurement of the penetration depths of red and near infrared light in human "ex vivo" tissues. *J. Photochem. Photobiol. B: Biology* **2000,** *57*, 90-93.

9. Shi, L.; Sordillo, L. A.; Rodríguez-Contreras, A.; Alfano, R., Transmission in near-infrared optical windows for deep brain imaging. *J. Biophotonics* **2016,** *9*, 38-43.

10. Romano, G.; Conti, A.; Fusi, F., Laser-tissue interaction principles: beam penetration in tissue. *Energy for Health* **2010,** *5*, 10-11.

11. Laha, S. S.; Naik, A. R.; Kuhn, E. R.; Alvarez, M.; Sujkowski, A.; Wessells, R. J.; Jena, B. P., Nanothermometry Measure of Muscle Efficiency. *Nano Lett.* **2017,** *17*, 1262-1268.

12. Ximendes, E. C.; Rocha, U.; del Rosal, B.; Vaquero, A.; Sanz-Rodríguez, F.; Monge, L.; Ren, F.; Vetrone, F.; Ma, D.; García-Solé, J.; Jacinto, C.; Jaque, D.; Fernández, N., In Vivo Ischemia Detection by Luminescent Nanothermometers. *Adv. Healthc. Mater.* **2017,** *6*, 1601195.

13. Balabhadra, S.; Debasu, M. L.; Brites, C. D. S.; Ferreira, R. A. S.; Carlos, L. D., Upconverting Nanoparticles Working As Primary Thermometers In Different Media. *J. Phys. Chem. C* **2017,** *121*, 13962-13968.

14. Marciniak, L.; Pilch, A.; Arabasz, S.; Jin, D.; Bednarkiewicz, A., Heterogeneously Nd^{3+} doped single nanoparticles for NIR-induced heat conversion, luminescence, and thermometry. *Nanoscale* **2017,** *9*, 8288-8297.

15. Rocha, U.; da Silva, C. J.; Ferreira Silva, W.; Guedes, I.; Benayas, A.; Martínez Maestro, L.; Acosta Elias, M.; Bovero, E.; Van Veggel, F. C. J. M.; García Solé, J. A.; Jaque, D., Subtissue Thermal Sensing Based on Neodymium-Doped LaF_3 Nanoparticles. *ACS Nano* **2013,** *7*, 1188-1199.

16. Rocha, U.; Jacinto, C.; Kumar, K. U.; López, F. J.; Bravo, D.; Solé, J. G.; Jaque, D., Real-time deep-tissue thermal sensing with sub-degree resolution by thermally improved Nd^{3+}:LaF_3 multifunctional nanoparticles. *J. Lumin.* **2016,** *175*, 149-157.

17. Cortelletti, P.; Facciotti, C.; Cantarelli, I. X.; Canton, P.; Quintanilla, M.; Vetrone, F.; Speghini, A.; Pedroni, M., Nd^{3+} activated CaF_2 NPs as colloidal nanothermometers in the biological window. *Opt. Mater.* **2017,** *68*, 29-34.

18. Kolesnikov, I. E.; Golyeva, E. V.; Kurochkin, M. A.; Lähderanta, E.; Mikhailov, M. D., Nd^{3+}-doped YVO_4 nanoparticles for luminescence nanothermometry in the first and second biological windows. *Sens. Act., B* **2016,** *235*, 287-293.

19. Rakov, N.; Maciel, G. S., Near-infrared emission and optical temperature sensing performance of Nd^{3+}:SrF_2 crystal powder prepared by combustion synthesis. *J. Appl. Phys.* **2017,** *121* (11), 113103.

20. Benayas, A.; del Rosal, B.; Pérez-Delgado, A.; Santacruz-Gómez, K.; Jaque, D.; Hirata, G. A.; Vetrone, F., Nd:YAG Near-infrared Luminescent Nanothermometers. *Adv. Opt. Mater.* **2015,** *3*, 687-694.

21. Ortgies, D. H.; Teran, F. J.; Rocha, U.; de la Cueva, L.; Salas, G.; Cabrera, D.; Vanetsev, A.S.; Rähn, M.; Sammelselg, V.; Orlovskii, Y. V.; Jaque, D., Optomagnetic Nanoplatforms for In Situ Controlled Hyperthermia. *Adv. Funct. Mater.* **2018**, *28*, 1704434.

22. Villa, I.; Vedda, A.; Cantarelli, I. X.; Pedroni, M.; Piccinelli, F.; Bettinelli, M.; Speghini, A.; Quintanilla, M.; Vetrone, F.; Rocha, U.; Jacinto, C.; Carrasco, E.; Rodriguez, F. S.; Juarranz, A.; del Rosal, B.; Ortgies, D. H.; Gonzalez, P. H.; Sole, J. G.; Garcia, D. J., 1.3 mu emitting SrF_2:Nd^{3+} nanoparticles for high contrast in vivo imaging in the second biological window. *Nano Res.* **2015,** *8*, 649-665.

23. Quintanilla, M.; Cantarelli, I. X.; Pedroni, M.; Speghini, A.; Vetrone, F., Intense ultraviolet upconversion in water dispersible SrF_2:Tm^{3+},Yb^{3+} nanoparticles: the effect of the environment on light emissions. *J. Mater. Chem. C* **2015,** *3*, 3108-3113.
24. Skripka, A.; Marin, R.; Benayas, A.; Canton, P.; Hemmer, E.; Vetrone, F., Covering the optical spectrum through collective rare-earth doping of $NaGdF_4$ nanoparticles: 806 and 980 nm excitation routes. *Phys. Chem. Chem. Phys.* **2017,** *19*, 11825-11834.
25. Jiang, D.; Zhan, Y.; Zhang, Q.; Ma, F.; Su, L.; Tang, F.; Qian, X.; Xu, J., Nd,Y:CaF_2 laser crystals: novel spectral properties and laser performance from a controlled local structure. *CrystEngComm* **2015,** *17*, 7398-7405.
26. Sun, Z.; Mei, B.; Li, W.; Liu, X.; Su, L., Synthesis and optical characterizations of Nd,Y:CaF_2 transparent ceramics. *Opt. Mater.* **2017,** *71*, 35-40.
27. Pedroni, M.; Piccinelli, F.; Passuello, T.; Polizzi, S.; Ueda, J.; Haro-Gonzalez, P.; Maestro, L. M.; Jaque, D.; Garcia-Sole, J.; Bettinelli, M.; Speghini, A., Water (H_2O and D_2O) Dispersible NIR-to-NIR Upconverting Yb^{3+}/Tm^{3+} Doped MF_2 (M = Ca, Sr) Colloids: Influence of the Host Crystal. *Cryst. Growth Des.* **2013,** *13*, 4906-4913.
28. Scarabelli, L.; Grzelczak, M; Liz-Marzan, L. M., Tuning Gold Nanorod Synthesis through Prereduction with Salicylic Acid. *Chem. Mater.* **2013,** *25*, 4232-4238.
29. González-Rubio, G.; Díaz-Núñez, P.; Rivera, A.; Prada, A.; Tardajos, G.; González-Izquierdo, J.; Bañares, L.; Llombart, P.; MacDowell, L.G.; Alcolea Palafox, M.; Liz-Marzán, L.M.; Peña-Rodríguez, O.; Guerrero-Martínez, A., Femtosecond laser reshaping yields gold nanorods with ultranarrow surface plasmon resonances. *Science* **2017**, *358*, 640-644.
30. Iparraguirre, I.; Azkargorta, J.; Fernandez, J.; Balda, R.; Oleaga, A., Laser spectral dynamics of Nd^{3+} in CaF_2-YF_3 crystals. *J. Opt. Soc. Am. B* **1999,** *16*, 1439-1446.
31. Han, T. P.; Jones, G. D.; Syme, R., Site-selective spectroscopy of Nd^{3+} centers in CaF_2:Nd^{3+} and SrF_2:Nd^{3+}. *Phys. Rev. B* **1993,** *47*, 14706-14723.
32. Corish, J.; Catlow, C.; Jacobs, P.; Ong, S., Defect aggregation in anion-excess fluorites - dopant monomers and dimers. *Phys. Rev. B* **1982,** *25*, 6425-6438.
33. Bausá, L. E.; Camarillo, E.; Garcia Sole, J.; Jaque, F.; Legros, R.; Munozyague, A., Site selection spectroscopy in CaF^2-Nd^{3+} films grown by molecular-beam epitaxy. *Solid State Commun.* **1993,** *85* (3), 257-261.
34. Voron'ko, Y. K.; Kaminskii, A. A.; Osiko, V. V., Analysis of the optical spectra of CaF_2:Nd^{3+} (Type 1) crystals. *Sov. Phys. - JETP* **1966,** *22*, 295 - 300.
35. Quintanilla, M.; Cantelar, E.; Cusso, F.; Villegas, M.; Caballero, A. C., Temperature sensing with up-converting submicron-sized $LiNbO_3$:Er^{3+}/Yb^{3+} particles. *Appl. Phys. Express* **2011,** *4*, 022601.
36. del Rosal, B.; Ximendes, E.; Rocha, U.; Jaque, D., In Vivo Luminescence Nanothermometry: from Materials to Applications. *Adv. Opt. Mater.* **2017,** *5*, 1600508.
37. Fodor, L.; Elman, M.; Ullmann, Y., Light Tissue Interactions. In *Aesthetic Applications of Intense Pulsed Light*, Springer-Verlag London: London, 2011; p 133.
38. Keijzer, M.; Jacques, S. L.; Prahl, S. A.; Welch, A. J., Light distributions in artery tissue: Monte Carlo simulations for finite-diameter laser beams. *Lasers Surg. Med.* **1989,** *9*, 148-154.
39. M. Maestro, L.; Haro-Gonzalez, P.; Sanchez-Iglesias, A.; Liz-Marzan, L. M.; García Solé, J.; Jaque, D., Quantum Dot Thermometry Evaluation of Geometry Dependent Heating Efficiency in Gold Nanoparticles. *Langmuir* **2014,** *30*, 1650-1658.

Table of Contents graphic: